Journal of
Marine Science and Engineering

MDPI

Article

Energy Characteristics in the Flow Channel of the Shaft-Type Tubular Pumping Station Considering Tides

Yufan He [1,2], Can Luo [1,2,*], Li Cheng [1,*], Yandong Gu [1] and Bin Gu [3]

[1] College of Hydraulic Science and Engineering, Yangzhou University, Yangzhou 225009, China; mz120211069@stu.yzu.edu.cn (Y.H.); guyandong@yzu.edu.cn (Y.G.)
[2] Engineering Research Center of High-Efficiency and Energy-Saving Large Axial Flow Pumping Station, Yangzhou 225009, China
[3] Hangzhou Regional Center (Asia-Pacific) for Small Hydro Power/National Research Institute for Rural Electrification, Hangzhou 310012, China; fdkkjfdjfc@163.com
* Correspondence: luocan@yzu.edu.cn (C.L.); chengli@yzu.edu.cn (L.C.)

Abstract: The shaft-type tubular pumping station has the remarkable characteristics of a large flow rate and high efficiency. It can realize the functions of irrigation, pumping, and drainage through pumping and generating conditions considering tides. Moreover, it is widely used in the plain area of eastern China and the tidal area along the marine region. Due to the different topological features of the airfoil of the impeller, the energy evolution characteristics of the shaft-type tubular pumping station during pumping and generating conditions remain unclear. The entropy generation theory was introduced to numerically simulate the flow pattern and energy characteristics in the shaft-type channel, impeller, and straight channel in operation conditions. The results show that the flow pattern is stable when the shaft-type channel and the straight-type channel are used as the inlet channel under pumping and generating conditions, and a low-pressure region occurs in the contraction section of the shaft-type channel. The velocity of sections of the inlet and outlet and the middle section of the impeller in the generating condition is larger than that in the pumping condition. In addition, the difference in the static pressure on the blade surface nearby the hub is large. With a change in the position of the wingspan, the difference gradually decreases from the small flow condition to the large flow condition. There is a high-entropy production rate zone in the channel contraction section and the shaft-type wall surface of the shaft-type flow channel. When the straight-type channel is used as the outlet flow channel, a high-entropy production region appears near the inlet water surface. In the pumping condition, a high-entropy production area is found at the inlet of the impeller, the blade groove channel, and the inlet of the guide vane. In the generating condition, a high-entropy production area is found at the out-of-impeller outlet, the blade groove channel, and the outlet of the guide vane. These research achievements have some reference value for the design of the shaft-type tubular pumping station considering tides and the study of hydraulic performance, along with the energy characteristics of the channels.

Keywords: shaft-type tubular pumping station; hydraulic performance; numerical simulation; experimental study; energy loss; entropy generation

check for updates

Citation: He, Y.; Luo, C.; Cheng, L.; Gu, Y.; Gu, B. Energy Characteristics in the Flow Channel of the Shaft-Type Tubular Pumping Station Considering Tides. *J. Mar. Sci. Eng.* **2024**, *12*, 607. https://doi.org/10.3390/jmse12040607

Academic Editor: Eugen Rusu

Received: 25 February 2024
Revised: 18 March 2024
Accepted: 26 March 2024
Published: 31 March 2024

1. Introduction

The eastern coastal area in China is flat and the altitude is low. Most of the large pumping stations for irrigation, pumping, and drainage are low-head pumping stations. The shaft-type tubular pumping station has been widely used for its low head and large flow rate. In addition, the shaft-type tubular pumping station is a reversible machine, which can be operated in both forward and negative directions [1,2]. Figure 1 shows how a shaft-type tubular pumping station operates under different operating conditions. In areas where the water level along the ocean is greatly affected by tides, it can not only pump in the forward direction but also generate electricity in the opposite direction. This pump device directly places the motor in the shaft-type, with a simple structure, small plane size, easy maintenance, and low construction cost [3]. The position of the shaft-type channel determines whether the shaft-type tubular pumping station is front-type or rear-type. Additionally, the majority of front shaft pumps have been used in the design since their hydraulic performance and flow pattern are superior to those of rear shaft-type pumping stations [4].

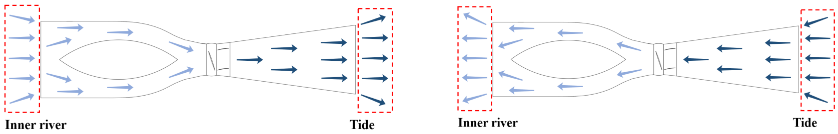

(a) pumping condition (b) generating condition

Figure 1. Operating condition diagram of a shaft-type tubular pumping station.

According to the CFD method, a large amount of research work has been carried out by Chinese and foreign researchers on the shaft-type tubular pumping station [5,6]. Xu, L. [7] noted that the hydraulic performance of this type of pumping station was superior by conducting a thorough analysis of the shaft-type tubular pumping station, revealing the correlation between the internal and external characteristics of the vertical mixed flow pump device to enhance its optimization using hydraulic design theory. Lu, W. [8] used a model experiment on an ultra-low lift pump station to investigate hydraulic performance under various blade angles, and based on this, plotted comprehensive characteristic curves and unit runaway speed curves for both the model and prototype pump devices. Yang, F. [9,10] discovered that the one-dimensional hydraulic design method is particularly effective for designing the inlet channel of tubular pumping stations. Additionally, it was found that variations in the shaft-type profile significantly influence the internal flow dynamics within these stations. Shi, L. [11] optimized the design of the two-way shaft-type tubular pumping station combined with the Longshan hydraulic project, showing that the internal and external contours of the bifurcation section of the shaft-type flow channel have a great influence on the hydraulic loss of the flow channel. Lin, P. [12] used the CFD method to study the force of shaft-type tubular pumping stations under the influence of different numbers of guide vanes, finding that setting the guide vane number to an even number can reduce the radial resultant force acting on the guide vanes. Zhang, R. [13] analyzed the flow loss performance of the shaft-type tubular pump station under different flow conditions by using the entropy production theory, revealing that the flow losses ranked from large to small in the order of impeller, outlet flow channel, guide vane, and inlet flow channel. Qian, Z. [14] investigated the impact of inlet and outlet flow channels, as well as front guide vanes, on the hydraulic performance of a tubular pumping station, determining that the distance between the shaft tail and the impeller center has the greatest influence on the velocity uniformity of the outlet section within the inlet channel. Luo, C. [15] performed numerical simulations to explore how different shaft-type transitions affect inflow efficiency and hydrodynamic performance at the entrance of shaft-type tubular pumping stations. The research, further supported by experimental validation, identified an optimal transition configuration. The findings indicate a consistent and smooth flow pattern in the inlet channel across various conditions, with the pump's high-efficiency zone typically extending from 0.9Qd to 1.2Qd. Cheng, K. [16] studied the hydraulic characteristics of the shaft-type tubular pumping station under different blade angles through model tests, finding that when the blade angle is 4°, the efficiency of the best efficiency point of the pumping device is the highest at 79.75%. Ji, D. [17] conducted a comparative analysis of the hydraulic efficiency and pressure pulsation traits of front and rear shaft-type tubular pumping stations, employing both numerical simulations and physical model tests. Their research revealed that the hydraulic efficiency of the pump device is largely determined by the characteristics of the outlet channel. Jiao, H. [18] studied the influence of front guide vanes on the pressure pulsation of the shaft tubular pumping device and discovered that the front guide vane may enhance the water inlet condition of the impeller and decrease pressure fluctuations on the blade surface. Xu, L. [19] studied the energy characteristics of the front shaft-type tubular pumping station at the inlet angles of two guide vanes, with the aim of increasing the pump station's efficiency. The studies revealed that the angle of the guide vane's inlet section plays an important role in the energy efficiency of pump devices. Lin, Z. [20] found the flow dynamics within the impeller of shaft-type tubular pumping stations under varying operational flows, focusing on phenomena such as tip gap leakage and changes in pressure pulsation. The findings showed an initial increase followed by a decrease in the amplitude of pressure pulsation at the tip clearance as the flow rate escalates. Furthermore, Meng, F. [21] explored the impact of a backflow gap on the energy efficiency of tubular pumping stations, employing the concept of entropy generation as a metric for energy dissipation. The empirical data, corroborated by tests, indicate that backflow clearance induces additional head loss, necessitating increased shaft power for the motor rotor's rotation. Previous studies on shaft-type tubular pumping stations have mostly focused on hydraulic performance, flow pattern, etc., under pumping conditions. This research compares the performance of a shaft-type tubular pumping station under both pumping and generating conditions, from the perspective of energy dissipation losses.

Taking a shaft-type tubular pump station nearby a marine region as an example, this paper uses the CFD numerical simulation method to analyze and study the energy characteristics of the shaft-type tubular pumping station considering tides. The relevant results have a certain application value for the operation of the shaft-type tubular pumping station nearby a marine region.

2. Numerical Simulation Methods

2.1. Governing Equations

The water flow in the shaft-type tubular pumping station follows the principles of momentum and mass conservation. For incompressible flows, in this paper, the continuity equation is expressed as [22]:

$$\frac{\partial(\rho u_i)}{\partial x_i} = 0 \tag{1}$$

The momentum equation is expressed as:

$$\frac{\partial}{\partial x_j}(\rho u_i u_j) = -\frac{\partial p^*}{\partial x_i} + \frac{\partial\left[\mu_{eff}\left(\frac{\partial u_i}{\partial x_j} + \frac{\partial u_j}{\partial x_i}\right)\right]}{\partial x_j} \tag{2}$$

$$\mu_{eff} = \mu + \mu_t \tag{3}$$

$$p^* = p + \frac{2}{3}\rho k \tag{4}$$

where u_i represents the three-dimensional velocity component of the fluid, x_i represents the three-dimensional coordinate component, p represents fluid pressure, ρ represents fluid density, and μ_{eff} represents the effective viscosity coefficient, which is equal to the sum of the molecular viscosity coefficient μ and the Boussinesq eddy viscosity coefficient μ_t.

The SST k-ω turbulence model, which corrects the turbulent viscosity formula, improves the transfer of shear stress at the wall surface. It helps anticipate flow nearby the wall and avoids over-predicting turbulent viscosity [23].

2.2. Entropy Production Theory

The theory of entropy generation has been applied to examine the distribution of flow energy loss within shaft-type tubular pumping stations [24,25]. Entropy production, which transforms the mechanical energy lost by the system into internal energy, is a dissipation effect brought on by irreversible factors in the process. Poor flow conditions within the pump system, including phenomena like flow separation and vortex generation, contribute to increased entropy production. This is also the case with the conversion of kinetic and pressure energy into internal energy, further emphasizing the significance of managing flow dynamics to enhance the energy efficiency of the system. The entropy production resulting from heat transfer is not taken into consideration in this research due to the comparatively large specific heat capacity of water.

The main entropy production in a turbulent flow field is the sum of time-averaged entropy production, fluctuating entropy production, and wall entropy generation. The calculation formula is as follows:

Time-averaged entropy production $\dot{S}'''_{\overline{D}}$:

$$\dot{S}'''_{\overline{D}} = \frac{\mu}{T}\left\{2\left[\left(\frac{\partial \overline{u}}{\partial x}\right)^2 + \left(\frac{\partial^2 \overline{v}}{\partial y}\right)^2 + \left(\frac{\partial^2 \overline{w}}{\partial y}\right)^2\right] + \left[\left(\frac{\partial \overline{v}}{\partial x} + \frac{\partial \overline{u}}{\partial y}\right)^2 + \left(\frac{\partial \overline{w}}{\partial x} + \frac{\partial \overline{u}}{\partial z}\right)^2 + \left(\frac{\partial \overline{v}}{\partial z} + \frac{\partial \overline{w}}{\partial y}\right)^2\right]\right\} \quad (5)$$

Fluctuating entropy production $\dot{S}'''_{D'}$:

$$\dot{S}'''_{D'} = \beta \frac{\rho \omega k}{T} \quad (6)$$

Wall entropy production $\dot{S}''_{W}$:

$$\dot{S}''_{W} = \frac{\vec{\tau}_W \cdot \vec{v}_W}{T} \quad (7)$$

Main entropy production $\dot{S}'''_{D}$:

$$\dot{S}'''_{D} = \dot{S}'''_{\overline{D}} + \dot{S}'''_{D'} + \dot{S}''_{W} \quad (8)$$

where μ represents dynamic viscosity, Pa·s; u, v, and w are time average speed, m/s; T represents Kelvin temperature, K; β represents an empirical constant, approximately 0.09; ρ represents fluid density, kg/m^3; ω represents turbulent eddy current frequency; k represents turbulent kinetic energy, s^{-1}; $\vec{\tau}_W$ represents wall shear stress, Pa; and $\vec{v}_W$ represents the velocity at the center of the first grid node near the wall surface, m/s.

2.3. Computational Domains

This research is modeled as a front shaft-type tubular pumping station. Figure 2 provides a detailed display of the parameters in the computational domain. The calculation domain comprises a shaft-type channel, impeller, guide vane, and straight-type channel, in which the impeller diameter is 300 mm, the impeller is 3 pieces, and the guide vane is 5 pieces. Extending both the import and export of computational domains helps to improve the stability of energy performance and flow characteristics. In this paper, the external characteristic curve between the extended boundary conditions and common boundary conditions are compared, their results show the same trend and a tiny difference. Therefore, extended boundary conditions are not adopted in this research. The length, width, and height of the shaft-type flow channel are 5.67D, 2.78D, and 1.3D, respectively. The straight-type flow channel measures 6.16D in length, 2.78D in width, and 1.3D in height. Table 1 below contains a list of its primary design parameters.

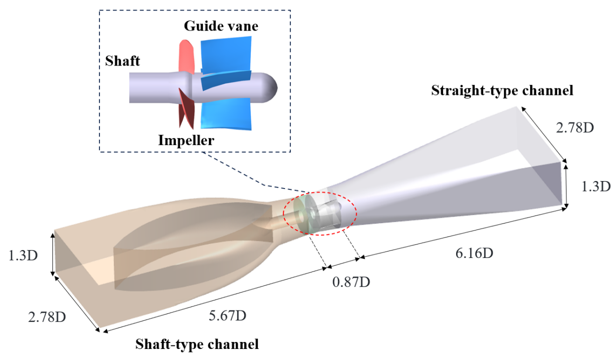

Figure 2. Computational domains.

Table 1. Main design parameters.

Parameter	Impeller Diameter D (mm)	Rotation Speed n (rev/min)	Design Flow Rate Q (L/s)	Blade Number
Value	300	1000	210	3

2.4. Grid Division

The ANSYS ICEM 19.2 platform is used to partition the computational domain of the impeller and guide the vane into structured mesh elements. As shown in Figure 3, the flow channel is spatially discretized using unstructured mesh elements with strong adaptability. The grid convergence verification of the GCI (Grid Convergence Index) standard based on the Richardson extrapolation method is adopted [26,27]. According to the standard grid refinement scale, three grid number schemes are selected, and the evaluation index is calculated to verify the grid convergence.

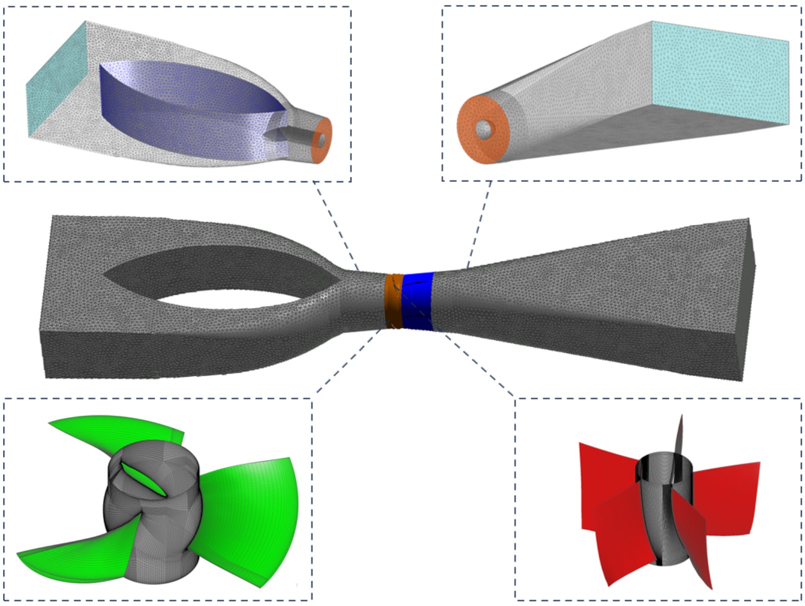

Figure 3. Mesh distribution.

Taking the design condition as an example, three groups of different grid number schemes of N_1 (1,087,016), N_2 (2,645,892), and N_3 (6,478,458) are set, respectively, and the grid refinement ratio is r_{21} (1.35) and r_{21} (1.35). The evaluation index selects the pump efficiency η [28]. In Table 2, both GCI values are less than 1. Moreover, the GCI value of N_3 is one-tenth of that of N_2, indicating that the grid discretization error of N_3 is small and has outstanding accuracy. The distribution of mesh elements within the shaft-type tubular pumping station is as follows: the shaft-type flow channel contains 901,154 mesh elements; the impeller region is composed of 1,835,248 mesh elements; the guide vane features 2,410,562 mesh elements; and the straight-type channel is equipped with 1,331,494 mesh elements.

Table 2. GCI value.

Total Number of Grid Nodes	r	η	$\lvert\varepsilon\rvert = \left\lvert\frac{\eta_k - \eta_{k+1}}{\eta_{k+1}}\right\rvert$	GCI = $\frac{1.25\lvert\varepsilon\rvert}{r^p - 1} \times 100$
1,087,016 (N_1)		0.76340		
2,645,892 (N_2)	1.35	0.76380	0.00482085	0.454037116
6,478,458 (N_3)	1.35	0.76750	0.00052370	0.049807763

2.5. Boundary Condition Settings

The setting of boundary conditions varies with different operation modes. The impeller blades are adjustable, but the guide vanes are not adjustable. The impeller speed is 1000 r/min in both pumping and generating conditions. During pumping conditions, the inlet of the shaft-type flow channel is designated as a mass flow inlet, while the outlet of the straight-type channel is assigned as a pressure outlet. Conversely, in the generating phase, the inlet of the straight-type channel assumes the role of a mass flow inlet, and the outlet of the shaft-type flow channel is defined as a pressure outlet. A 'stage' model is employed to address the static and dynamic interfaces of the 'impeller outlet-guide vane inlet' and 'shaft-type outlet-impeller inlet' interfaces, whereas the remaining interfaces are 'static'. The boundary condition for solid walls is established as non-slip, with a wall function being applied to the region adjacent to the wall. The criterion for convergence accuracy is specified as 1.0×10^{-4}.

2.6. Analysis Sections

In Figure 4, the cross-sections of the shaft-type tubular pumping station are sliced by intercepting the cross part of the flow channel, the inlet part of the impeller, the middle part of the impeller, and the inlet part of the guide vane in turn, recorded as section *n*–*n* (*n* = 1~4). Sections 5~7 are wingspan surfaces, which are span = 0.05, span = 0.5, and span = 0.95, respectively.

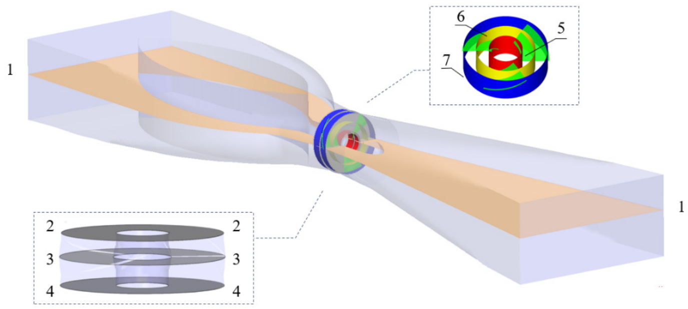

Figure 4. Cross-section selection.

3. Experimental Verifications

Figure 5 shows the performance curve of the shaft-type tubular pumping station under various conditions. A dimensionless treatment of the flow is carried out, and the calculation formula of the dimensionless flow is as follows:

$$Q_{\mathrm{d}} = \frac{Q_i}{Q_{\mathrm{des}}} \tag{9}$$

where Q_i is the flow rate of the pumping station at the working condition and Q_{des} is the pumping station's flow rate that corresponds to the pump's design working point.

When the pumping condition switches to the generating condition, the rotation direction of the impeller changes from clockwise rotation to counterclockwise rotation, the head of the impeller becomes the tail of the impeller, and the pressure side becomes the suction side. In Figure 5, the shaft-type tubular pumping station has a maximum efficiency of 78% under pumping conditions, and as the flow rate increases, the head steadily declines. When the pumping station enters the generating condition, the head gradually increases with the increase in the flow rate, and the highest point efficiency is 79.7%. At the same time, it is observed that the high-efficiency range of the pumping station is notably broader compared with that under pumping conditions.

Table 3 presents a comparison between the results of numerical simulations and model tests conducted under pumping conditions. This comparison reveals that the overall trend in the data acquired from both numerical simulations and model testing under designed flow conditions aligns closely. It is found that the overall trend in the data obtained by numerical simulation and the model test under the design flow condition is basically the same. The Mean Absolute Percentage Error (MAPE) of head and efficiency is 9.1% and 1.0%, respectively. In general, a smaller MAPE value indicates that the average deviation between the calculated results of the model and the experimental values is small, indicating that the prediction accuracy is high. When the numerical simulation is carried out, the roughness is not set near the wall in the boundary condition, so the numerical simulation results are different from the experimental data under various flow conditions, especially under large flow conditions.

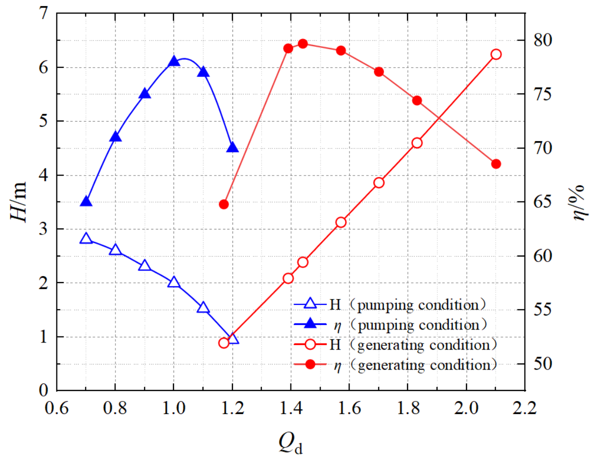

Figure 5. Bidirectional operation performance curve of the shaft-type tubular pumping station.

Table 3. Comparison between the results of numerical simulations and model experiments.

Flow condition	0.7Q	0.8Q	0.9Q	1.0Q	1.1Q	1.2Q
Experimental head (m)	2.64	2.39	2.12	1.79	1.41	1.08
Numerical head (m)	2.81	2.60	2.31	2.00	1.53	0.95
MAPE (%)	9.1					
Experimental efficiency (%)	66.22	73.12	74.54	77.89	77.55	69.81
Numerical efficiency (%)	65.40	71.78	75.11	78.23	77.22	70.85
MAPE (%)	1.0					

4. Results Analysis

4.1. Flow Pattern Analysis

Based on the operational efficiency of the pump, flow rates of 0.8Q, 1.0Q, and 1.2Q are selected to analyze the flow characteristics under the pumping condition [20]. According to the generating condition, 0.9Q, 1.1Q, and 1.4Q are selected as the low flow conditions, design flow conditions, and large flow conditions, respectively.

Figures 6 and 7 show the pressure cloud contour and streamline contour of the cross-section 1-1 under pumping and generating conditions. Figure 6a–c show that the overall flow pattern in the shaft-type flow channel is good under various flow conditions, with water flowing uniformly into two streams. The streamline and pressure are symmetrically distributed along the shaft-type flow channel. As the cross-section of the shaft-type flow channel shrinks, the flow on either side diminishes, leading to a steady increase in the flow rate while the pressure within the channel gradually decreases. Notably, there exists a small region of low-pressure areas just outside the trailing edge of the shaft-type flow channel. Owing to the confluence of the tail of the shaft-type flow channel into a stream of water, the pressure and velocity change rapidly, and the velocity toward the inside is less than the outside. The low-pressure area vanishes as the flow rate increases and the static pressure area grows from the trailing edge to the middle edge to the inlet, with an increasing range of variation. The vortex appears in the central part of the straight-type flow channel, where the flow pattern is more disorganized, and no low-pressure area is seen. As shown in Figure 7a–c, the straight-type flow channel under the generating condition is evenly distributed as the streamline of the inlet flow channel, and the water flow is divided into two streams, which flow smoothly through the guide vane. At the time, the shaft-type flow channel does not exhibit the phenomena of flow separation. The flow of water flows through the section contracting, causing the outer velocity to exceed the inner velocity. As a result, there are symmetric high- and low-pressure areas from within and outside the shaft-type channel and the trailing edge of the impeller. When the flow rate increases, the low-pressure area outside the trailing edge fades away, and the pressure gradient shift phenomena in the static pressure area spreads from the trailing edge of the flow channel to the middle edge.

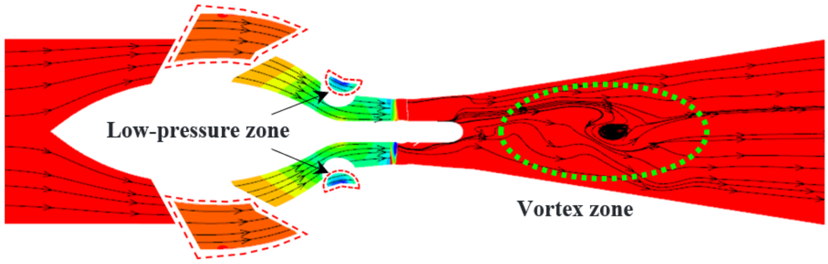

(**a**) 0.8Q

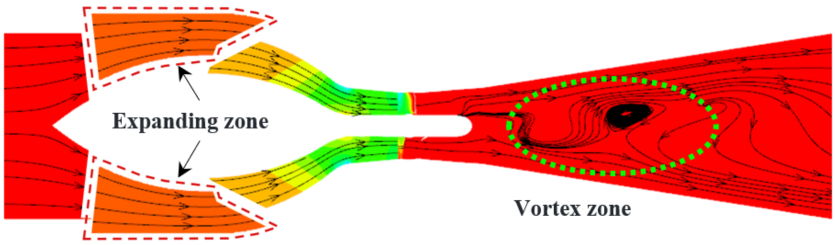

(**b**) 1.0Q

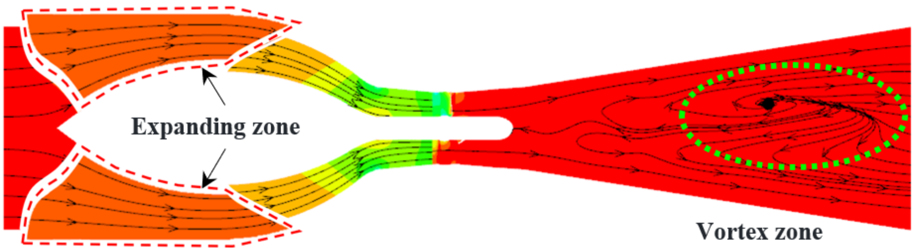

(**c**) 1.2Q

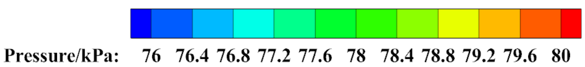

Figure 6. Pressure contour and streamline contour under pumping conditions.

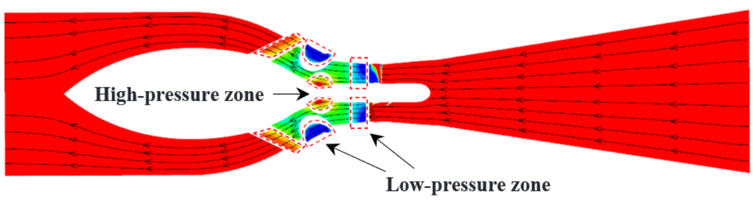

(**a**) 0.9Q

Figure 7. *Cont.*

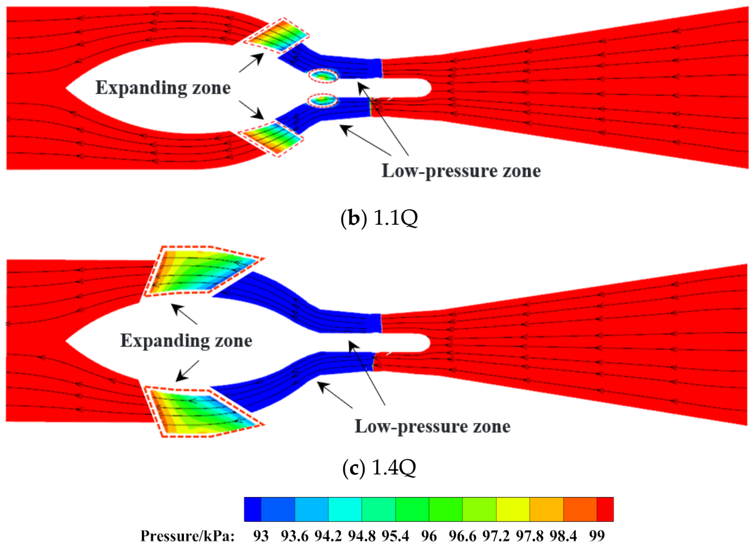

Figure 7. Pressure contour and streamline contour under generating conditions.

4.2. Distribution of Flow Velocity and Pressure Characteristics of Impeller

Figure 8 shows axial velocity contour of section 2-2. Notably, in cross-section 2-2, the patterns of velocity distribution for each operational condition show significant variations between the pumping and generating conditions, attributable to the impeller's different rotational directions in each condition. Under all operating conditions, the velocity at the blade groove channel is less than the blade velocity, and the velocity close to the impeller's suction side is overly large. As the flow rate increases, the blade's velocity changes more significantly, and the water flow velocity during the generating condition is higher than that during the pumping condition.

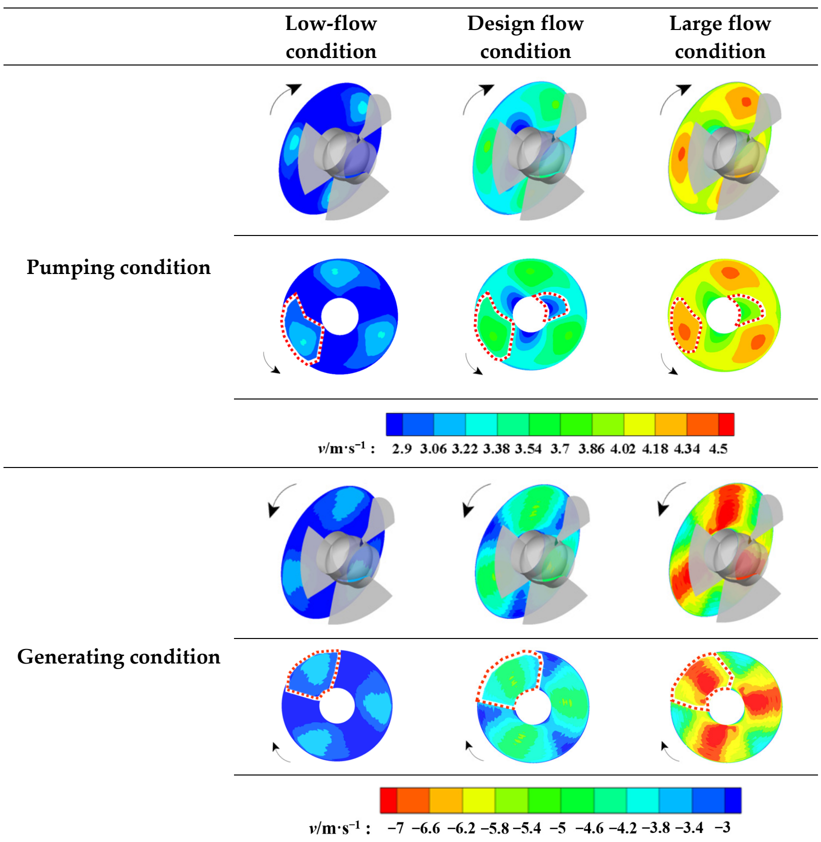

Figure 8. Axial velocity contour of section 2-2.

Figure 9 presents axial velocity contour of section 3-3. In section 3-3, the center part of the impeller during bidirectional operation has almost the same velocity distribution. Furthermore, under small flow circumstances, the low-speed zone is substantially bigger than the high-speed zone. The high-speed zone's range gradually extends as its flow velocity rises. Meanwhile, the change range of the high-speed zone under the generating condition is greater than that under the pumping condition, and the small velocity zone appears on the edge side of the blade.

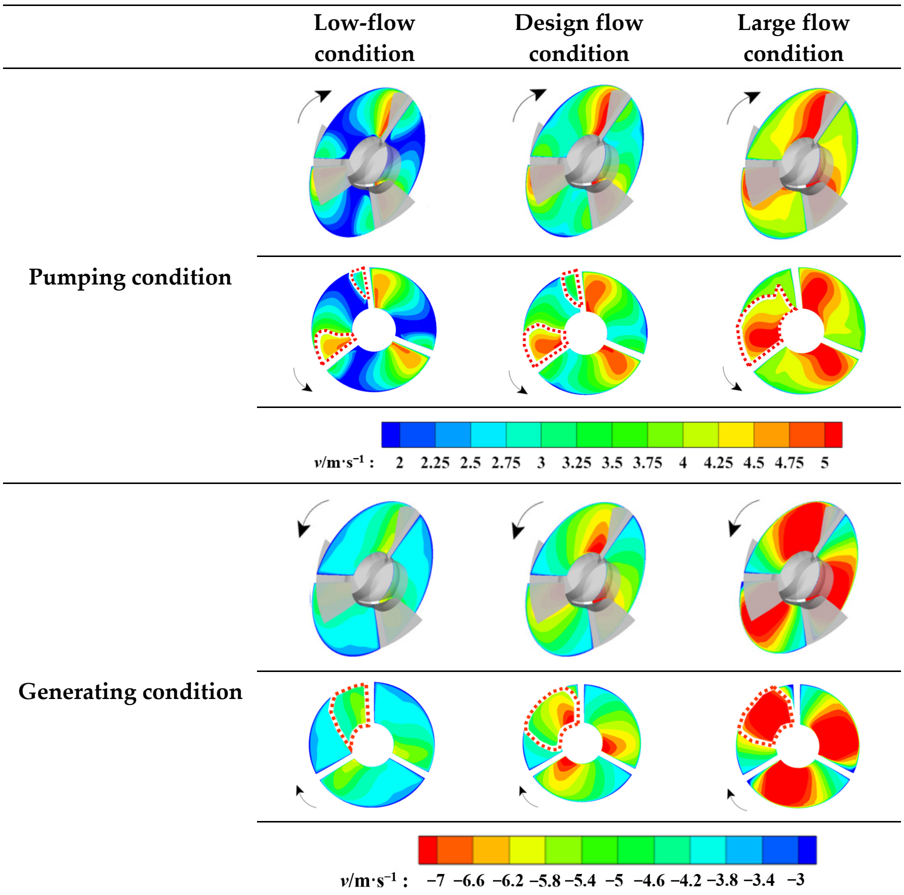

Figure 9. Axial velocity contour of section 3-3.

Figure 10 shows axial velocity contour of section 4-4. In section 4-4, the velocity distribution of each working condition under the pumping condition is obvious, which is similar to section 2-2. While the low-velocity area close to the wall gradually decreases, the inlet side's velocity is larger than the outlet side's, and its value rises as the flow rate increases.

There is a close relationship between the performance of a pump and the pressure characteristics on the pressure and suction sides of the blades. The collaboration between the high-pressure zone on the pressure side and the low-pressure region on the suction side propels the flow through the pump. Analyzing the static pressure distribution on the blades can provide insights into the pressure characteristics affecting the impeller during operating conditions. As observed in Figures 11 and 12, the flow conditions during the pumping and generating conditions are used as the study object to determine the static pressure distribution on various wingspans of impeller blades. The chordwise position is represented by the vertical axis, x/l, and the blade surface's static pressure is represented by the longitudinal axis. The positions of the wingspan are as follows: span = 0.05 (near the hub), span = 0.5 (the middle section of the impeller), and span = 0.95 (near the shroud). In the figure, the upper side is the static pressure curve of the pressure side, and the lower side is the suction side.

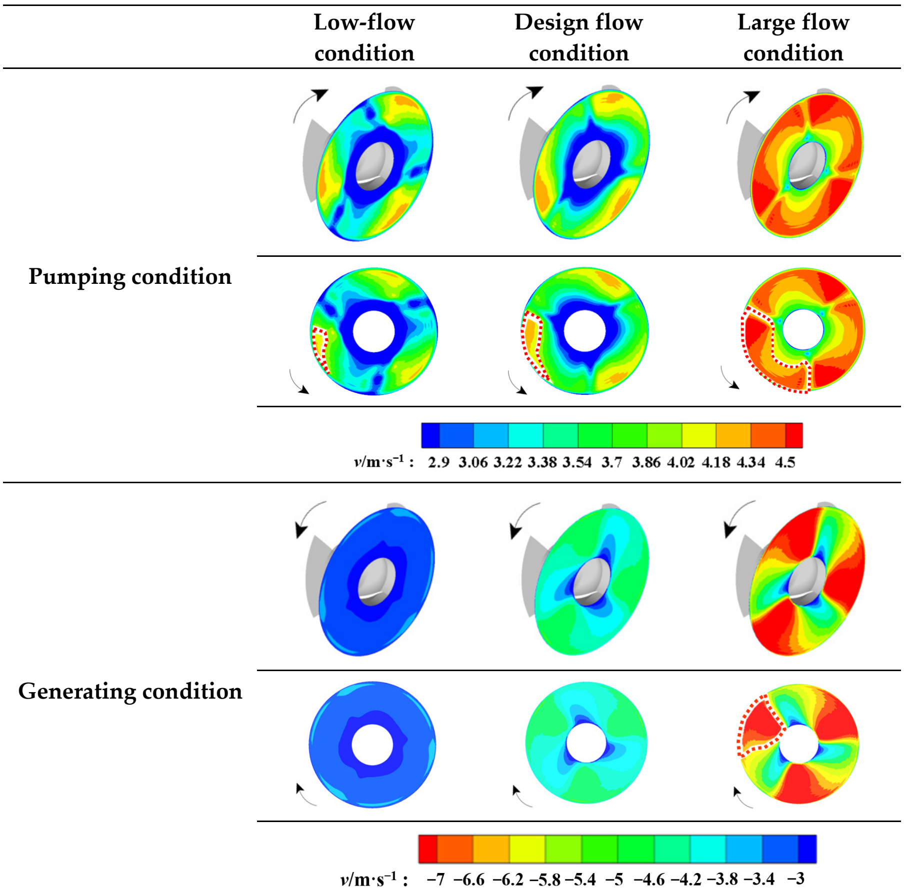

Figure 10. Axial velocity contour of section 4-4.

Figure 11 shows the static pressure distribution of different spans under pumping conditions. The figure displays that in the axial direction of the flow, the static pressure is greatest nearby the blade's leading edge. The effect of the flow rate creates a large static pressure differential between the suction and pressure surfaces of the blade at span = 0.05 under pumping conditions. The static pressure difference is largest at low-flow conditions, and the pressure difference reaches the maximum near x/l = 0.5, indicating that the flow pattern in the blade groove is disordered and the flow characteristics are different. On the other hand, there is a negligible static pressure differential between the blade's pressure surface and suction surface for span = 0.5 and span = 0.95. The pressure values of each wingspan surface are not much different when x/l is greater than 0.5, indicating that the flow characteristics in the blade groove are basically the same. Simultaneously, when comparing various flow conditions, it becomes apparent that while there are significant differences in the pressure surfaces across different wingspans, the value of the pressure difference remains unaffected by increases in flow rate. This observation indicates that changes in flow rate predominantly affect the numerical values on the pressure surface without altering its inherent pattern of change.

Figure 12 shows the static pressure distribution of different spans under generating conditions. The static pressure curves of the pressure surface and the suction surface of each wingspan near x/l = 0.05 have different degrees of crossover with different flow rates. The impeller's power is significantly diminished since it is dependent on the static pressure differential between the blade's suction and pressure surfaces to function. Under conditions of high flow, there is a significant static pressure difference between the suction surface close to the hub position and the local pressure surface, as well as a significant flow differential. Both under low-flow and design flow conditions, the pressure surface and suction surface of each wing surface exhibit a static pressure curve trend that is essentially the same, with values that are roughly comparable.

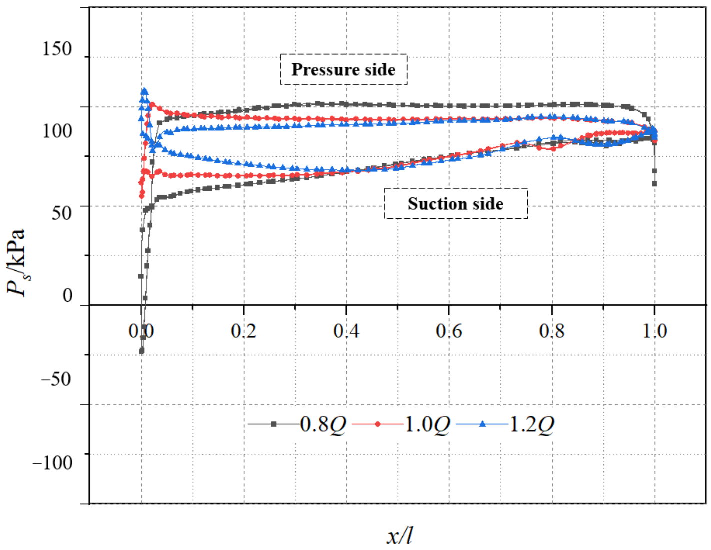

(**a**) span = 0.05

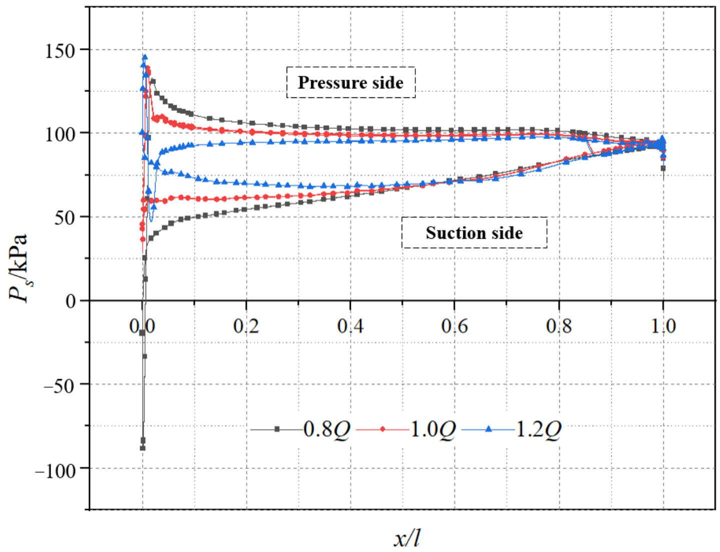

(**b**) span = 0.5

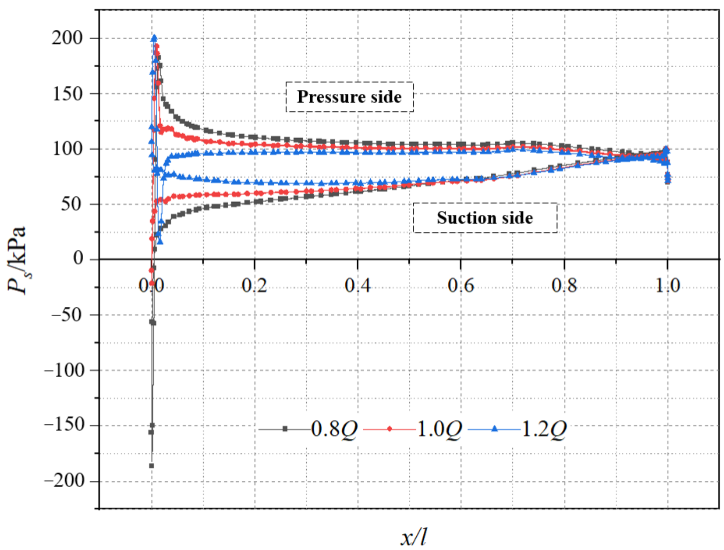

(**c**) span = 0.95

Figure 11. The static pressure distribution of different spans under pumping conditions.

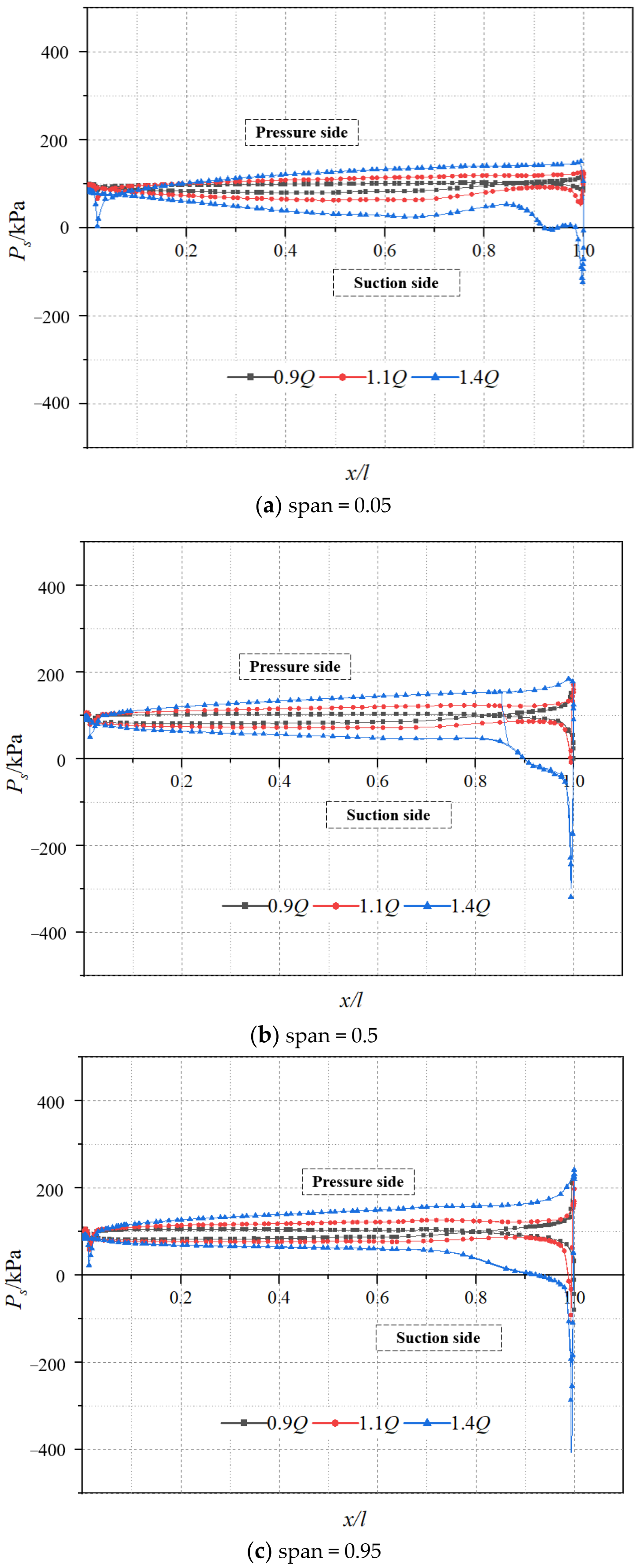

Figure 12. The static pressure distribution of different spans under generating conditions.

4.3. Energy Entropy Generation Characteristics

Figures 13 and 14 depict the entropy production rates within the shaft-type and straight-type channels under various operational conditions. As is shown in Figure 13, there is no high-entropy production zone from the inlet to the middle edge of the shaft-type in the pumping condition, while there is a gradually increasing high-entropy production area from the middle edge of the shaft-type wall to the trailing edge. The re-convergence of the water flow, which was previously divided by a shaft-type owing to the progressive shrinkage of the flow channel, is the source of this energy loss. The energy loss results from the water flow re-convergent, which is induced by the shaft-type separation under the effect of the gradual contraction of the flow channel. A high-entropy production area is generated on the outer wall of the inlet surface of the flow channel, and the water flow is squeezed to the wall after the diversion during the generating condition, forming a gradually decreasing high-entropy production area on the wall of the shaft-type. The data indicate that during both the pumping and generating conditions, the majority of the energy loss of the shaft-type flow channel occurs at the converging part of the flow channel and the shaft-type wall. Figure 14 illustrates that during pumping conditions, when the straight-type flow channel serves as the outlet, water flow through the guide vanes is deflected, leading to a disorganized flow pattern. Moreover, the condition results in a high-entropy generation area emerging near the inlet surface of the channel. With the increase in the flow rate, the flow pattern on the inlet side of the flow channel is relatively stable, resulting in a gradual disappearance of the region of high-entropy production. When under the generating condition, the straight-type flow channel is used as the inlet flow channel, which has smooth water flow with no high-entropy production region. This indicates that the energy loss in the straight-type flow channel is related to the water flow pattern.

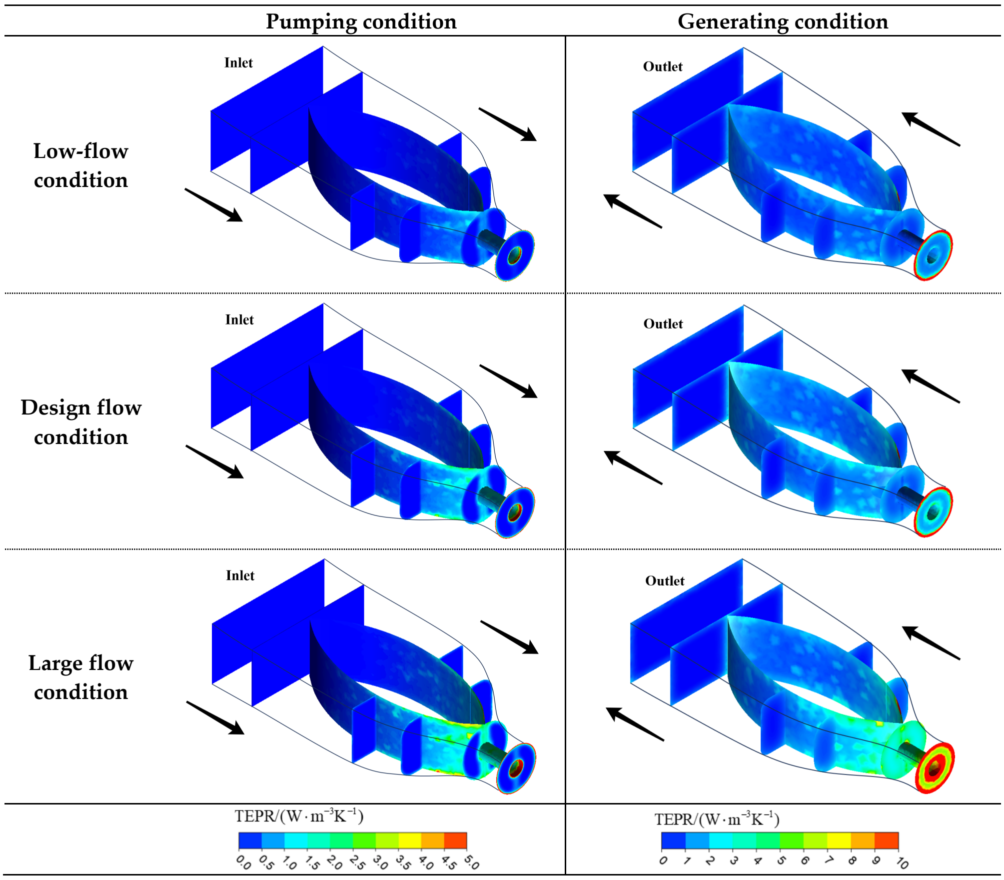

Figure 13. The entropy generation rate of the shaft-type flow channel for different flow conditions.

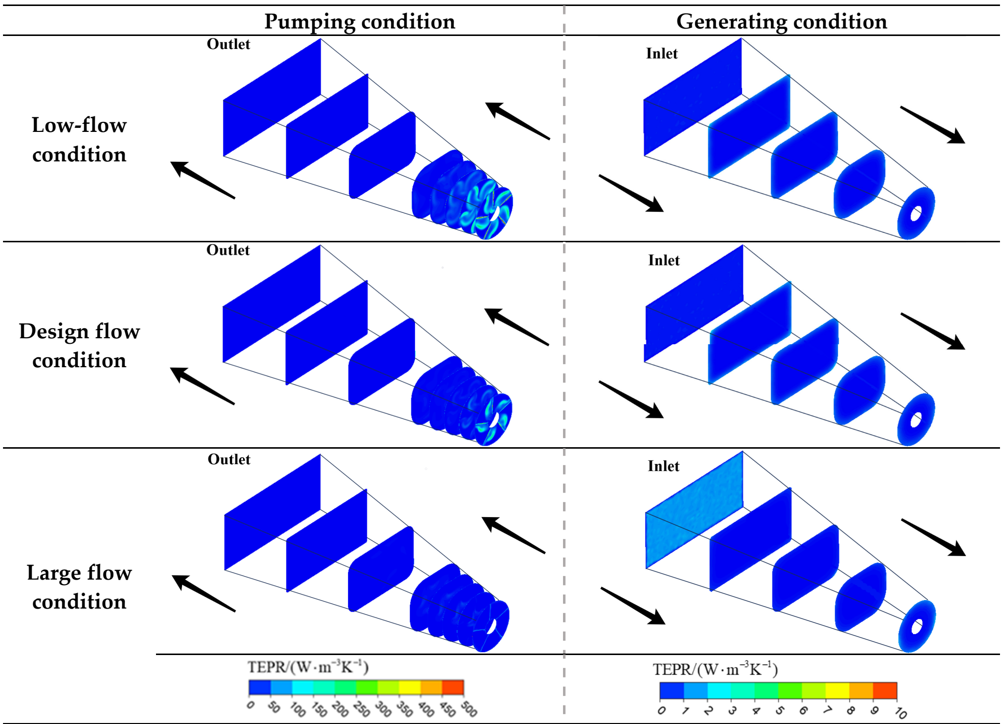

Figure 14. The entropy generation rate of the straight-type flow channel for different flow conditions.

Figure 15 shows the entropy generation rate diagram of the impeller under various operation conditions. Figure 15a shows that high entropy generation appears near the inlet. When compared with low-flow conditions, design flow conditions and high-flow conditions further extend the region of high entropy generation around the suction surface. The hub-side suction exhibits strong regional entropy generation at both its trailing and front edges, as seen in Figure 15b. As the flow rate increases, the region of high entropy generation moves toward the blade channel and eventually dissipates at the trailing edge. This shows that the energy loss of each operation condition under pumping conditions mainly occurs near the impeller inlet and the blade groove channel. In the generating condition, there is a high-entropy production area on the inlet of the impeller on the shroud side, as shown in Figure 15a, which occupies the whole blade groove channel at high-flow conditions. In Figure 15b, the hub-side blade suction surface has a large entropy generation area at its center edge. The high entropy generation area is mostly seen in the blade channel along with the impeller outlet as the flow rate increases, suggesting that these locations would generate the majority of the energy loss associated with each operating state during the generating condition.

Figure 16 illustrates the entropy generation rate of the guide vane under various operational conditions. In the pumping conditions, as depicted in Figure 16a, a high-entropy production zone is evident near the inlet surface on the shroud side of the guide vane. Conversely, under low-flow conditions, this high-entropy production zone is located at the front edge of the blade's suction side, which diminishes as the flow rate escalates. This pattern indicates that, under pumping conditions, the primary locations of energy loss occur near the inlet surface of the guide vane and within the blade groove channel. Specifically, from the front edge to the middle edge of the blade, the high-entropy production region on the shroud side expands along the groove channel with an increasing water flow rate, particularly prominent at the blade suction's front edge, as shown in Figure 16a. Figure 16b reveals that the area of high-entropy production on the hub concentrates around the groove channel and expands across the entire hub surface with an increase in flow rate. According to this, during generating conditions, it is deduced that the guide vane outlet and the blade groove channel are the main sites of energy loss.

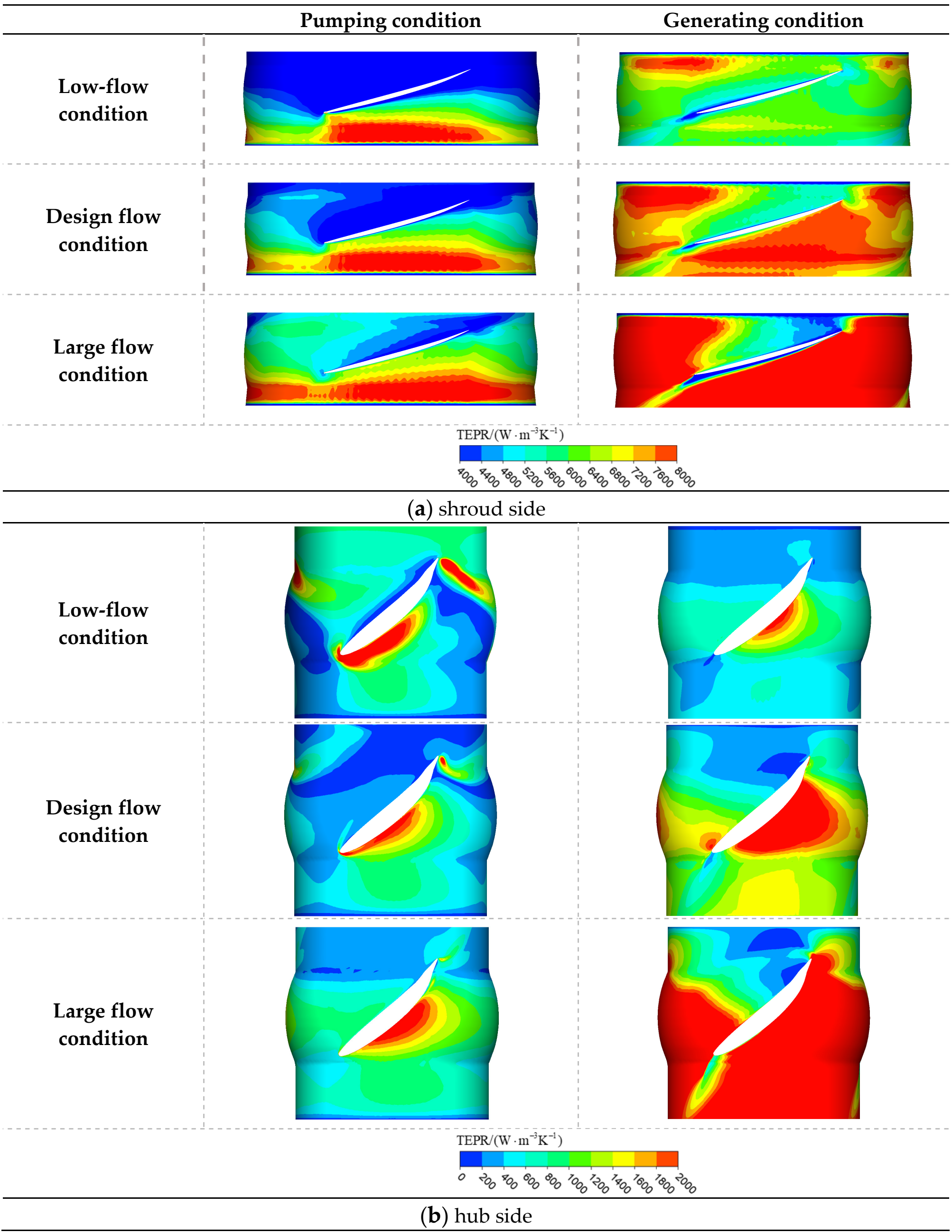

Figure 15. The entropy generation rate of the impeller with different flow conditions.

Figures 17–19 are the entropy generation rate diagram of cross-sections 2-2, 3-3, and 4-4 in various flow conditions. The diagrams analyze the distribution of the entropy production rate in each section by comparing the relative positions of the impeller rotation under each operating condition. In Figure 17, section 2-2 is the inlet surface of the impeller in the pumping condition. Additionally, in the low-flow rate condition, there is a tiny area of significant entropy formation along the blade's trailing edge. In addition, there is almost no high-entropy production area and almost no energy loss with a large flow rate. In the generating condition, section 2-2 serves as the outlet surface of the impeller, and as the flow rate increases, the high-entropy production area is mainly concentrated at the leaf groove channel and at the edge of the blade, along with increasing energy loss. Figure 18 shows that the entropy production distribution of section 3-3 and section 2-2, which represent the center part of the impeller, is essentially the same. In the pumping condition, there is a little amplitude of a high-entropy production area on the side of the inner wall, which disappears with a large flow rate. Conversely, when the flow rate increases in the generating condition, the high-entropy generation region is mostly centered on the blade's edge. In Figure 19, section 4-4 is the impeller outlet surface in the pumping condition. The range of the high-entropy generation area rapidly narrows and is located in the blade leading edge as well as the blade groove channel along with an increasing flow rate.

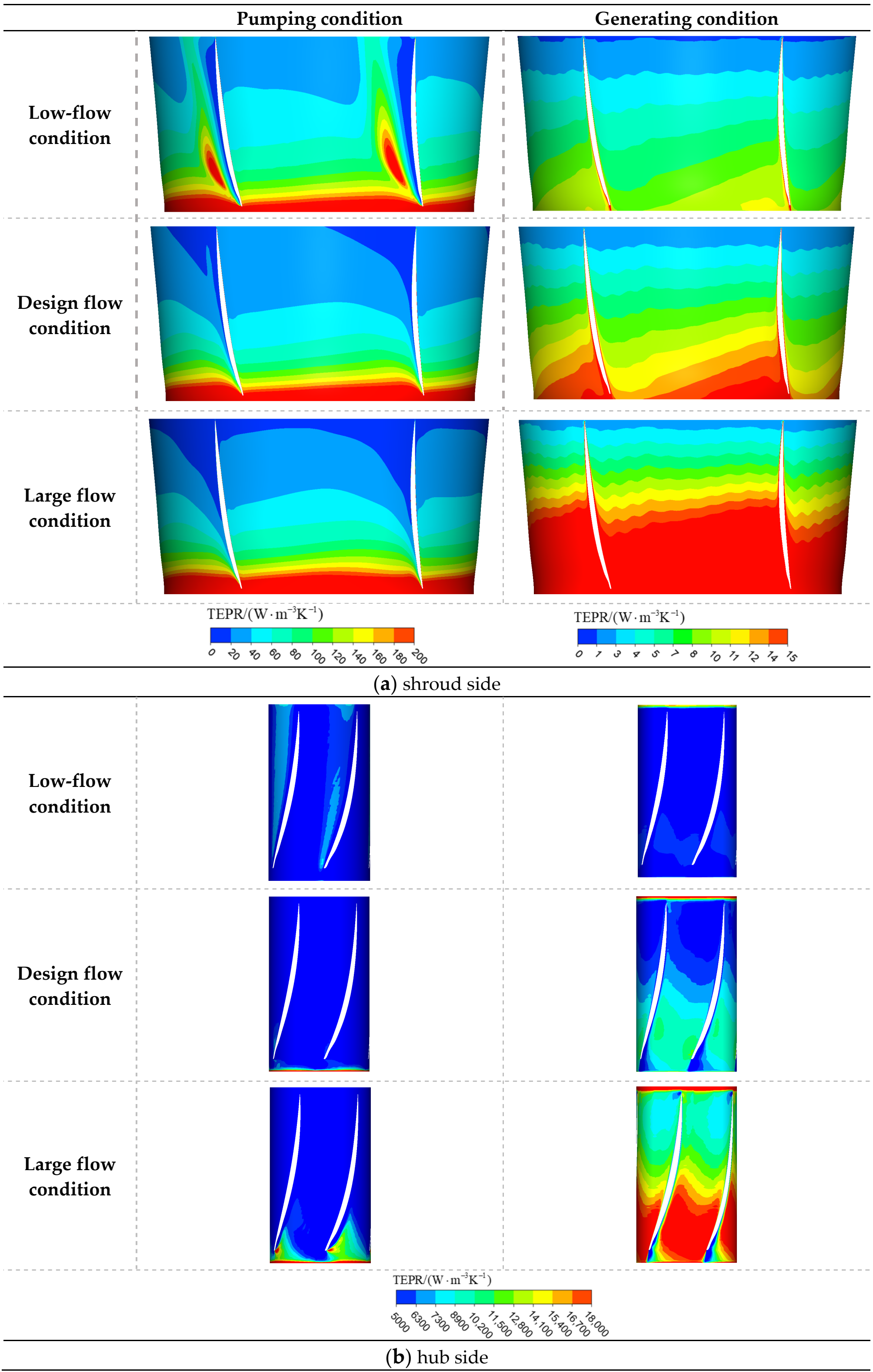

Figure 16. The entropy generation rate of the guide vane with different flow conditions.

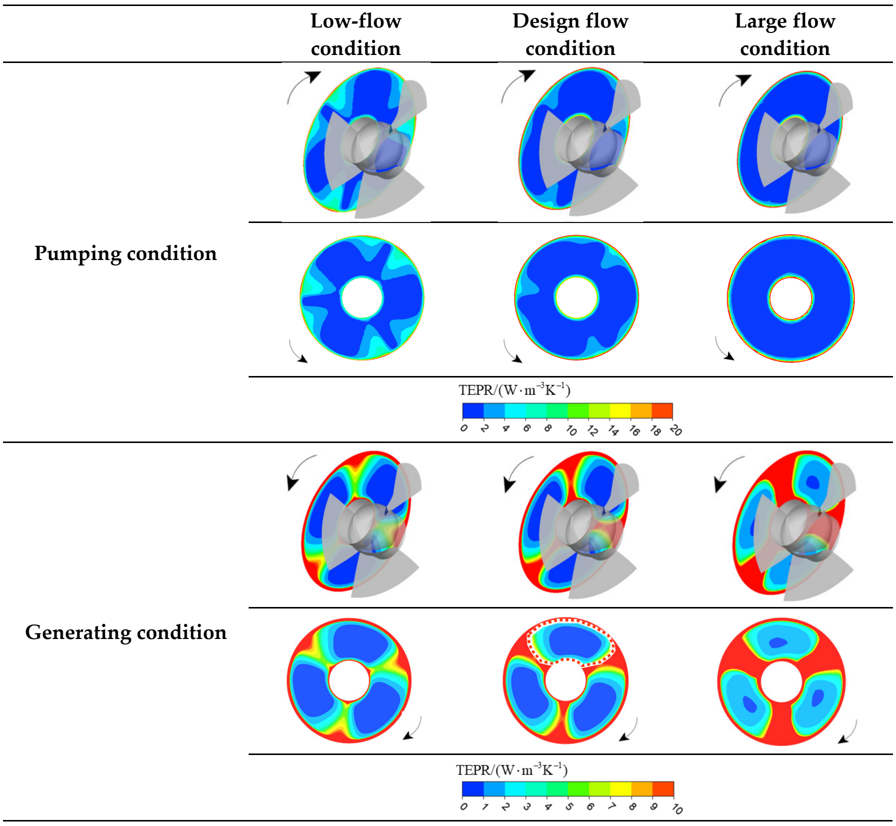

Figure 17. The entropy production rate of section 2-2 under different flow conditions.

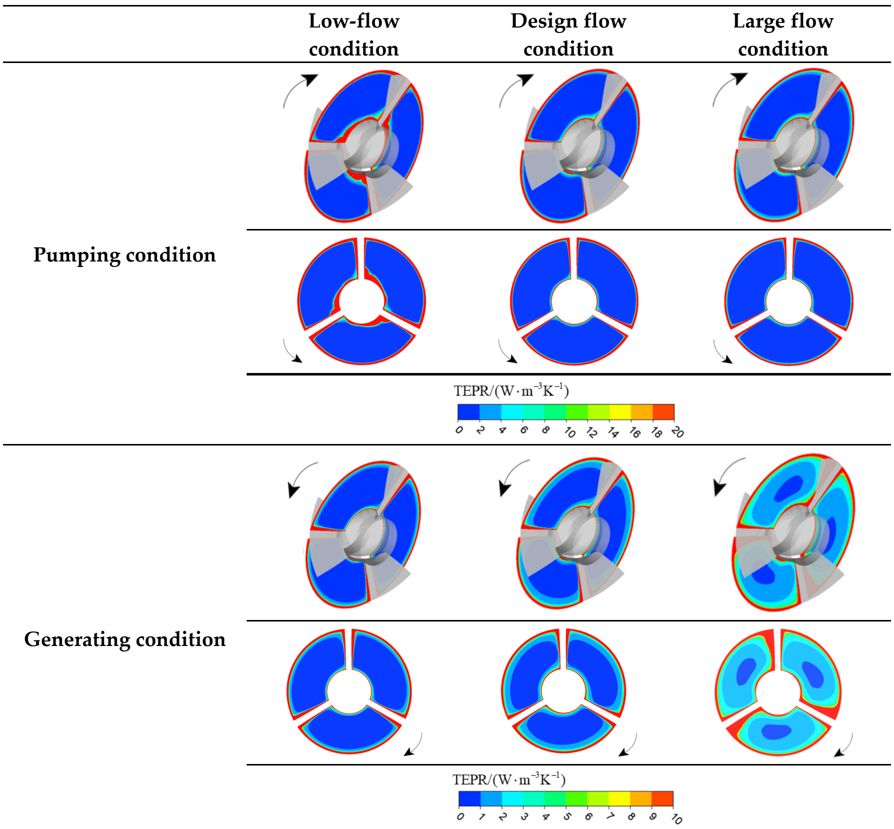

Figure 18. The entropy production rate of section 3-3 under different flow conditions.

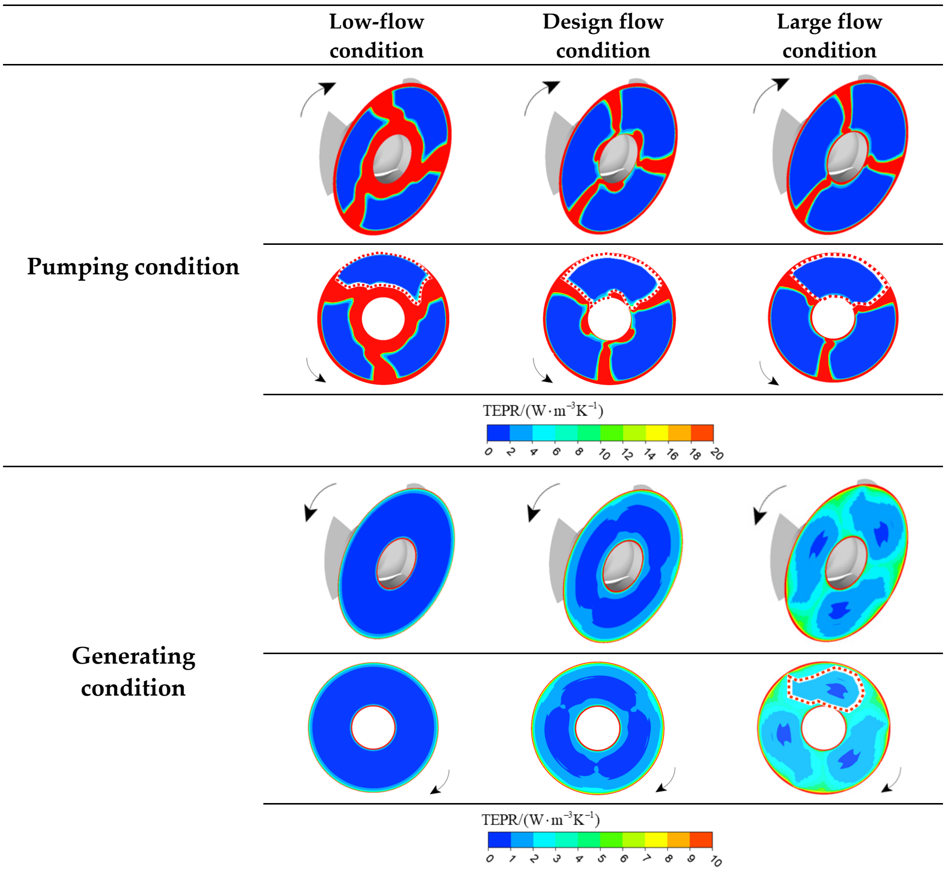

Figure 19. The entropy production rate of section 4-4 under different flow conditions.

5. Conclusions

Through the numerical simulation of the hydraulic performance of a shaft tubular pumping station, the hydraulic characteristics under bidirectional operating conditions are analyzed. The conclusions are as follows:

(1) The flow in the shaft-type channel is smooth, and the overall flow pattern is rather uniform during the pumping condition. During the contraction section of the shaft-type flow channel, a low-pressure zone forms that extends to the center edge of the shaft. As the flow rate increases, this range does as well. There is a vortex in the center of the straight-type flow channel, which squeezes the water flow, while the flow pattern in the channel is disordered without the existence of a low-pressure zone. Under the generating condition, the straight-type flow channel is used as an inlet flow channel with a good flow pattern. Upon the water's smooth passage into the shaft-type flow channel, a low-pressure area can be observed near to the constriction portion. The change in the trend is consistent with the pressure distribution region during advancement.

(2) Compared with the pumping condition, the impeller's flow velocity is higher during the generating condition. On the leading edge of the blade, there is a zone of high speed, and as the flow rate increases, the range gradually gets wider.

(3) As the flow rate increases, the static pressure differential between the impeller blade surface's suction and pressure surfaces gets progressively reduced, enhancing the flow characteristics in the blade groove channel.

(4) By analyzing the energy loss of the entire pumping station, it is found that the high-entropy production area is mainly centralized in the convergent section of the flow channel and the wall surface of the shaft-type when the shaft-type flow channel is used as the inlet and outlet flow channels, respectively. There is almost no energy loss when the straight-type flow channel is used as the inlet flow channel. When

functioning as the outlet channel, a high-entropy production area emerges near the inlet surface, attributed to the turbulence of the water flow. Mainly at the impeller inlet and the blade groove channel during the pumping condition is the high-entropy generation rate location at the impeller. In addition, under the generating condition, the impeller outlet and the blade channel are the primary locations of the high-entropy generation region. With the increase in flow rate, this area gradually expands to cover 80% of the blade groove channel. Furthermore, when under pumping conditions, the guide vane's zone of high entropy production is mostly focused on its inlet side; conversely, when operating in reverse, the region of high entropy production is primarily concentrated on its outlet side. The area expands and covers 50% of the blade groove channel under high-flow conditions.

Author Contributions: Data curation, Y.H. and C.L.; methodology, L.C. and Y.G.; formal analysis, Y.H.; writing—original draft, Y.H.; writing—review and editing, B.G., C.L. and L.C.; supervision, C.L. All authors have read and agreed to the published version of the manuscript.

Funding: This research was funded by the Open Project Program of Engineering Research Center of High-efficiency and Energy-saving Large Axial Flow Pumping Station of Jiangsu Province (Grant no. ECHEAP026), the Postgraduate Research and Practice Innovation Program of Jiangsu Province (Grant no. SJCX22_1759), the National Natural Science Foundation of China (Grant no. 52279091), Jiangsu Province Science Foundation for Youths of China (Grant no. BK20170507), the Natural Science Foundation of the Jiangsu Higher Education Institutions of China (Grant no. 17KJD580003), Jiangsu Planned Projects for Postdoctoral Research Funds of China (Grant no. 1701189B), and Priority Academic Program Development of Jiangsu Higher Education Institutions of China (PAPD).

Institutional Review Board Statement: Not applicable.

Informed Consent Statement: Not applicable.

Data Availability Statement: All data is available in this paper.

Acknowledgments: The authors thank the College of Hydraulic Science and Engineering, Yangzhou University. The author is very grateful for discussions with C.L. and K.D. A huge thanks is due to the editor and reviewers for their valuable comments to improve the quality of this paper.

Conflicts of Interest: The authors declare no conflicts of interest.

References

1. Liu, C. Researches and developments of axial-flow pump system. *Nongye Jixie Xuebao/Trans. Chin. Soc. Agric. Mach.* **2015**, *46*, 49–59. [CrossRef]
2. Yang, J.; Fang, G.; Hu, D.; Cai, Z.; Zhai, J.; Zheng, Y.; Kan, K. Hydrodynamic and structura1 stabi1ity analysis for shaft type tubular pump unit. *IOP Conf. Ser. Earth Environ. Sci.* **2021**, *647*, 012038. [CrossRef]
3. Jin, K.; Chen, Y.; Tang, F.; Shi, L.; Liu, H.; Zhang, W. Influence of shaft type location on hydraulic characteristics of bidirectional tubular pump systems. *J. Hydroelectr. Eng.* **2021**, *40*, 67–77. [CrossRef]
4. Chen, S.; Yan, H.; Zhou, Z.; He, Z.; Wang, L. Three-dimensional turbulent numerical simulation and model test of front-shaft type tubular inlet conduit of pumping station. *Trans. Chin. Soc. Agric. Eng.* **2014**, *30*, 63–71. [CrossRef]
5. Landvogt, B.; Osiecki, L.; Patrosz, P.; Zawistowski, T.; Zylinski, B. Numerical simulation of fluid-structure interaction in the design process for a new axial hydraulic pump. *Prog. Comput. Fluid Dyn. Int. J.* **2014**, *14*, 31–37. [CrossRef]
6. Lucius, A.; Brenner, G. Numerical Simulation and Evaluation of Velocity Fluctuations During Rotating Stall of a Centrifugal Pump. *J. Fluids Eng.* **2011**, *133*, 081102. [CrossRef]
7. Xu, L.; Lu, L.; Chen, W.; Wang, G. Flow pattern analysis on inlet and outlet conduit of shaft type tubular pump system of Pizhou pumping station in South-to-North Water Diversion Project. *Trans. Chin. Soc. Agric. Eng.* **2012**, *28*, 50–56. [CrossRef]
8. Lu, W.; Zhang, X. Research on model test of hydraulic characteristics for super-low head shaft type well tubular pump unit. *J. Irrig. Drain.* **2012**, *31*, 103–106. [CrossRef]
9. Yang, F.; Liu, C.; Tang, F.; Cheng, L.; Lv, D. Numerical simulation of 3D internal flow and performance analysis of the shaft type tubular pump system. *J. Hydroelectr. Eng.* **2014**, *33*, 178–184. [CrossRef]
10. Yang, F.; Liu, C.; Tang, F.; Zhou, J. Shaft type shape evolution and analysis of its effect on the pumping system hydraulic performance. *J. Basic Sci. Eng.* **2014**, *22*, 129–139. [CrossRef]
11. Shi, L.; Liu, X.; Tang, F.; Yao, Y.; Xie, R.; Zhang, W. Design optimization and experimental analysis of bidirectional shaft type tubular pumping station. *Nongye Jixie Xuebao/Trans. Chin. Soc. Agric. Mach.* **2016**, *47*, 85–91. [CrossRef]

12. Lin, P.; Bai, Z.; Tang, F.; Zhang, Y.; Zhen, B.; Wang, Y. The influence of guide vanes on force imposed to bidirectional shaft type tubular pump. *J. Irrig. Drain.* **2023**, *42*, 82–89. [CrossRef]
13. Zhang, R.; Tan, S.; Ding, X.; Xu, H.; Feng, J.; Mou, T.; Fei, Z. Flow loss characteristics of a shaft type tubular pump based on entropy production theory. *Adv. Sci. Technol. Water Resour.* **2022**, *42*, 6–12. [CrossRef]
14. Qian, Z.; Zhou, X.; Jiao, H.; Xia, Z.; Chen, S. Research on the Channel and Front Guide Vane of the Shaft type Tubular Pump Unit Based on CFD. *China Rural Water Hydropower* **2022**, 101–106+112. Available online: https://link.cnki.net/urlid/42.1419.tv.20211215.1529.026 (accessed on 24 February 2024).
15. Luo, C.; Du, K.; Qi, W.; Cheng, L.; Huang, X.; Lu, J. Investigation on the effect of the shaft type transition form on the inflow pattern and hydrodynamic characteristics of the pre-shaft type tubular pumping station. *Front. Energy Res.* **2022**, *10*, 955492. [CrossRef]
16. Cheng, K.; Li, S.; Cheng, L.; Sun, T.; Zhang, B.; Jiao, W. Experiment on Influence of Blade Angle on Hydraulic Characteristics of the Shaft type Tubular Pumping Device. *Processes* **2022**, *10*, 590. [CrossRef]
17. Ji, D.; Lu, W.; Lu, L.; Xu, L.; Liu, J.; Shi, W.; Huang, G. Study on the Comparison of the Hydraulic Performance and Pressure Pulsation Characteristics of a Shaft type Front-Positioned and a Shaft type Rear-Positioned Tubular Pumping stations. *J. Mar. Sci. Eng.* **2022**, *10*, 8. [CrossRef]
18. Jiao, H.; Sun, C.; Chen, S. Analysis of the influence of inlet guide vanes on the performance of shaft type tubular pumps. *Shock Vib.* **2021**, *2021*, 5177313. [CrossRef]
19. Xu, L.; Lv, F.; Li, F.; Ji, D.; Shi, W.; Lu, W.; Lu, L. Comparison of energy performance of shaft type tubular pumping station at two guide vane inlet angles. *Processes* **2022**, *10*, 1054. [CrossRef]
20. Lin, Z.; Yang, F.; Guo, J.; Jian, H.; Sun, S.; Jin, X. Leakage Flow Characteristics in Blade Tip of Shaft type Tubular Pump. *J. Mar. Sci. Eng.* **2023**, *11*, 1139. [CrossRef]
21. Meng, F.; Li, Y.; Pei, J. Energy characteristics of full tubular pumping station with different backflow clearances based on entropy production. *Appl. Sci.* **2021**, *11*, 3376. [CrossRef]
22. Chen, J.; Su, Z.; Wang, M.; Pu, J.; Chen, S. Numerical analysis of hydraulic characteristics of shaft tubular pump set. *China Rural Water Hydropower* **2018**, *7*, 152–157.
23. Wang, F. *Analysis Method of Flow in Pumps and Pumping Stations*; China Water Power Press: Beijing, China, 2020.
24. Kock, F.; Herwig, H. Local entropy production in turbulent shear flows: A high-Reynolds number model with wall functions. *Int. J. Heat Mass Transf.* **2004**, *47*, 2205–2215. [CrossRef]
25. Zhao, W.; Zhang, J.; Yu, X.; Zhou, D.; Calamak, M. Multiobjective optimization of a tubular pump to improve the applicable operating head and hydraulic performance. *Proc. Inst. Mech. Eng. Part C J. Mech. Eng. Sci.* **2021**, *235*, 1555–1566. [CrossRef]
26. Gu, Y.; Sun, H.; Wang, C.; Lu, R.; Liu, B.; Ge, J. Effect of Trimmed Rear Shroud on Performance and Axial Thrust of Multi-Stage Centrifugal Pump With Emphasis on Visualizing Flow Losses. *J. Fluids Eng.* **2024**, *146*, 011204. [CrossRef]
27. Celik, I.; Ghia, U.; Roache, P.; Freitas, C. Procedure for estimation and reporting of uncertainty due to discretization in CFD applications. *J. Fluids Eng.* **2008**, *130*, 078001. [CrossRef]
28. Guo, Q. Study on the Characteristics of the Blade Tip Leakage Vortex Flow and the Cavitating Flow Field. Ph.D. Thesis, China Agricultural University, Beijing, China, 2017.